Hydrol. Earth Syst. Sci. Discuss., 7, 6351–6380, 2010
www.hydrol-earth-syst-sci-discuss.net/7/6351/2010/
doi:10.5194/hessd-7-6351-2010

Hydrology and Earth System Sciences Discussions

Rainfall retrievals over West Africa using SEVIRI: evaluation with TRMM-PR and monitoring of the daylight time monsoon progression

E. L. A. Wolters[1], **B. J. J. M. van den Hurk**[1,2], **and R. A. Roebeling**[1]

[1]Royal Netherlands Meteorological Institute (KNMI), P.O. Box 201, 3730 AE De Bilt, The Netherlands
[2]Institute for Marine and Atmospheric Research Utrecht (IMAU), Utrecht University, P.O. Box 80000, 3508 TA Utrecht, The Netherlands

Received: 22 July 2010 – Accepted: 16 August 2010 – Published: 27 August 2010

Correspondence to: E. L. A. Wolters (wolterse@knmi.nl)

Published by Copernicus Publications on behalf of the European Geosciences Union.

Abstract

This paper describes the application of the KNMI cloud physical properties – precipitation properties (CPP-PP) algorithm over West Africa. The algorithm combines condensed water path (CWP), cloud phase (CPH), cloud particle effective radius (r_e), and cloud-top temperature (CTT) information, retrieved from visible, near-infrared and infrared observations of the Spinning Enhanced Visible and Infrared Imager (SEVIRI) onboard Meteosat-9 to estimate precipitation occurrence and intensity. It is investigated whether the CPP-PP algorithm is capable of retrieving rain occurrence and intensity over West Africa with a sufficient accuracy, using tropical monsoon measurement mission precipitation radar (TRMM-PR) and a small number of rain gauge observations as reference. As a second goal, it is assessed whether SEVIRI is capable of monitoring both the seasonal and synoptical evolution of the West African monsoon (WAM). It is shown that the SEVIRI-detected rainfall area agrees well with TRMM-PR, having a correlation coefficient of 0.86, with the areal extent of rainfall by SEVIRI being ~10% larger than TRMM-PR. The mean retrieved rain rate from CPP-PP is about 8% higher than from TRMM-PR. The frequency distributions of rain rate reveal that the median rain rates of CPP-PP and TRMM-PR are similar. However, rain rates >7 mm h^{-1} are retrieved more frequently by SEVIRI than by TRMM-PR, which is partly explained by known biases in TRMM-PR. Finally, it is illustrated that both the seasonal and synoptical time scale of the WAM can be well detected from SEVIRI daytime observations. It was found that the daytime westward MCS travel speed fluctuates between 50 and 60 km h^{-1}. Furthermore, the ratio of MCS precipitation to the total precipitation was estimated to be about 27%. Our results indicate that rainfall retrievals from SEVIRI can be used to monitor the West African monsoon.

1 Introduction

Precipitation can be considered the most crucial link between the atmosphere and the surface in weather and climate processes. Quantitative precipitation estimates at high spatial and temporal resolution are of increasing importance for water resource management, for improving the precipitation prediction scores in numerical weather prediction (NWP) models, and for monitoring seasonal to interannual climate variability. A dense and high-temporal resolution ground-based measurement network is required to achieve accurate precipitation observations. However, in several regions, especially over the tropical land areas and over the oceans, the coverage by rain gauges and/or ground-based radars is insufficient. For example, over certain regions in West Africa only a few rain gauges per 1000 km^2 are available (Ali et al., 2005b). Satellite instruments, especially those onboard geostationary satellites, have the potential to alleviate this observational coverage problem.

The retrieval of rainfall intensity and rainfall amount from passive satellite imagery is closely related to the detection of convective cloud cells. Until now, many convection detection retrieval techniques have been developed (see e.g., Mecikalsi and Bedka, 2006; Zinner et al., 2008). Most precipitation schemes from passive imagery are based on the assumption that clouds start to precipitate if the retrieved cloud particle effective radius (r_e) or cloud-top temperature (CTT) becomes higher or lower than a certain threshold value, respectively. The rationale behind the latter is that precipitation is more likely to occur if water droplets and ice crystals coexist (Pruppacher and Klett, 1997). However, the relation between CTT and rain rate is indirect, since e.g. thick cirrus clouds also have low temperatures, but generally do not produce any (surface-observed) rain. Despite this drawback, various rainfall retrieval techniques have been based on thermal infrared (TIR) temperatures only (mostly using the 10–12 µm atmospheric window spectrum), assuming that the amount of non-precipitating cirrus clouds is only minor (Negri et al., 1984; Adler and Negri, 1988; Negri and Adler, 1993; Ba and Gruber, 2001). An advantage of TIR data is the availability during both day and night.

HESSD
7, 6351–6380, 2010

Title Page
Abstract | Introduction
Conclusions | References
Tables | Figures
◀ | ▶
◀ | ▶
Back | Close
Full Screen / Esc
Printer-friendly Version
Interactive Discussion

Although the performance of TIR-based rainfall retrieval algorithms is quite poor in estimating instantaneous rain rates, a good correlation between cloud-top temperature and rainfall is found when accumulated over large areas and sufficiently long time periods (Kidd, 2001). In this paper, a novel approach using cloud-top properties retrieved from visible and near-infrared reflectances will be used to estimate rain rate.

Local economy, hydrology, and ecology in Western Africa are heavily dependent on the availability of monsoon rains. Especially in a region northward of ~15° N, less monsoon rain during subsequent years may intensify desertification, although no significant trend has been found throughout the 1980s and 90s (Nicholson et al., 1998). Less rainfall during the monsoon season also results in an increased surface albedo (because of decreased soil moisture content), increased dust generation, and less agricultural yield. Therefore a continuous rainfall monitoring of great importance.

The West-African monsoon (WAM) is the northward movement of the Inter Tropical Convergence Zone (ITCZ) during boreal summer and is manifested by the convergence of moist southwesterly air from the Atlantic Ocean with dry northeasterly air from the Sahara, the latter generally being referred to as Harmattan. The start of the monsoon season is often determined by a change in sign of the zonal wind component (u), i.e., a change from a westward into an eastward component. With the start of the monsoon season, first some sporadic convective activity due to the advection of moist oceanic air is triggered. This usually occurs from mid-April to mid-May and is followed by a relatively dry spell of about one month. Subsequently, the full onset of the WAM sets in around the end of June. Sultan and Janicot (2003) found that this onset date is 24 June ±8 days for the period 1968–1990. After this onset, a band with westward moving mesoscale convective systems (MCSs) traverses northward over the West African continent. These MCSs are transported through African easterly waves (AEWs), which in turn are dynamical disturbances within the African easterly jet (AEJ). Satellite-based estimates of the relative amount of precipitation produced by large convective systems vary from ~22% (Laing et al., 1999) to ~90% (Mathon et al., 2002). Part of the differences between these estimates originate from the classification of these convective systems into different categories. The initiation of MCSs is not only dynamically driven, but is also dependent on e.g. soil wetness, with convection being suppressed over too wet soils (Taylor and Ellis, 2006; Taylor et al., 2007).

Often a sudden shift from ∼5° N to ∼10° N of the most heavy rains is seen after the onset date. Several mechanisms explaining the monsoon jump have been proposed. For example, Sultan and Janicot (2003) suggested that due to persistent heating of the land surface near 15° N a thermal low develops, which is gradually strengthened by upper-air divergence caused by the tropical easterly jet (TEJ). However, Ramel et al. (2006) debated this mechanism, as they posed that in the region near 15° N no sufficient low-level moisture is available to initiate large-scale wet convection. With the passage of the heavy monsoon rains, maximum convective activity occurs late in the afternoon, likely as a result of gravity waves from morning convection over the West African ocean propagating northward (Sultan et al., 2007). However, Basu (2007) noted a shift of the main convective activity during the monsoon towards the late night/early morning, especially when dynamical factors and/or orography are involved.

Due to the sparse distribution of rain gauges over West Africa, monitoring the movement of the monsoon rains is rather difficult. Rainfall estimates from geostationary satellite instruments might have the potential to improve this monitoring. At the Royal Netherlands Meteorological Institute (KNMI), an algorithm has been developed to estimate rainfall rates from satellite-retrieved cloud properties.

The aim of this paper is to assess whether the KNMI cloud physical properties – precipitation properties algorithm (CPP-PP) is suitable to accurately estimate rainfall over West Africa in terms of mean rainfall area and median rain rate. In a verification study by Roebeling and Holleman (2009) with ground-based radar over the Netherlands, the areal extent of rainfall as detected by CPP-PP from Spinning Enhanced Visible and Infrared Imager (SEVIRI) data correlates well (corr∼0.9) and the retrieved rain rates have an accuracy of about 11%. In this paper, rain rate retrievals from the Tropical Rainfall Measurement Mission precipitation radar (TRMM-PR) and a small number of rain gauge data are used as reference dataset. Secondly, we evaluate the ability

HESSD
7, 6351–6380, 2010

of the algorithm to monitor the various aspects of the WAM dynamics for the period May–September 2006. Hovmüller diagrams are constructed for both north–south and east–west directions to investigate the dynamical processes on monthly and synoptical time scales, respectively. Finally, we estimate the westward MCS travel speed and the fractional amount of precipitation produced by MCSs and compare our results to earlier estimates found in literature.

The paper is organized as follows. Section 2 presents the methodology and various datasets used. Section 3 contains the results and the discussion, and conclusions are drawn in Sect. 4.

2 Data and methods

2.1 Rainfall retrieval technique

SEVIRI, onboard the geostationary Meteosat-8 and Meteosat-9 satellites of the European Organization for the Exploration of Meteorological Satellites (EUMETSAT), is a passive imager with 11 operational narrowband channels in the spectral range 0.6–13.4 µm. Three spectral channels cover the visible and near-infrared, and the remaining eight cover the thermal infrared spectral region. The sampling resolution is 3×3 km^2 at nadir. SEVIRI scans the Earth every 15 min from southeast to northwest.

The rainfall retrieval algorithm used here was introduced by Roebeling and Holleman (2009). It has been adapted from a method originally developed for use on the special sensor microwave/imager (SSM/I) by Wentz and Spencer (1998) to make it suitable for use on SEVIRI data. The algorithm estimates rain rate using condensed water path (CWP), cloud particle effective radius (r_e), cloud geometric height (ΔH), and cloud thermodynamic phase (CPH) as retrieved using the cloud physical properties retrieval algorithm (CPP, Roebeling et al., 2006). The algorithm is operationally applied to reflectances and radiances observed by SEVIRI.

The CPP algorithm retrieves cloud optical thickness (τ), r_e, and CPH in an iterative way by comparing observed SEVIRI reflectances to pre-calculated lookup table (LUT) reflectances obtained from the doubling adding KNMI (DAK, Stammes, 2001; De Haan et al., 1987) radiative transfer model (RTM). CWP is proportional to the product of the retrieved τ and r_e values. The thermodynamic phase "water" or "ice" is assigned to those cloud flagged pixels for which the observed 0.6- and 1.6-µm reflectances matches the corresponding water or ice cloud LUT reflectances. If phase "ice" is assigned, an additional CTT check (obtained from 10.8 µm brightness temperatures) is applied to ascertain the cloud phase assignment. If CTT is >265 K, phase "ice" is changed into "water" (Wolters et al., 2008). It is noted that at low cloud fraction, τ and r_e can be significantly under- and overestimated, respectively (Wolters et al., 2010). For the present study, CPP retrievals are limited to solar and viewing zenith angles (θ_o and θ, respectively) <60°. For West Africa, observations between 7:30 and 16:30 UTC are within this limit. Throughout the investigated period (May–September 2006) there is only a minor shift in these times and we have thus applied this daytime period over the entire dataset.

The separation of precipitating from non-precipitating clouds is the first step in the retrieval of rain rates. Precipitating clouds are detected from CWP, r_e, and CPH information. Water cloud pixels with CWP values larger than 150 g m^2 and r_e values larger than 16 µm are flagged precipitating, while for ice clouds all pixels with CWP larger than 150 g m^2 are flagged precipitating. For the pixels that are flagged precipitating the rain rate is calculated using the following equation (Roebeling and Holleman, 2009):

$$R = \frac{c}{\Delta H}\left[\frac{\mathrm{CWP_a} - \mathrm{CWP_o}}{\mathrm{CWP_o}}\right]^{1.6}, \tag{1}$$

with $\mathrm{CWP_a}$ the actual condensed water path. $\mathrm{CWP_o}$ is an offset CWP value that is set at 125 g m^{-2}), the constant factor c has a value of 1 and is of unity mm h^{-1} km and ΔH

is the height of the rain column, which is defined as:

$$\Delta H = \frac{\mathrm{CTT_m} - \mathrm{CTT_a}}{\gamma} + dH, \tag{2}$$

in which $\mathrm{CTT_a}$ and $\mathrm{CTT_m}$ denote the CTT of the actual pixel and the maximum CTT in a 100×100 pixel area around the actual pixel, respectively. The pixel with maximum CTT is assumed to represent a low, thin cloud and thus gives an estimate of the cloud base. The denominator γ represents the mean wet adiabatic lapse rate of 6.0 K km^{-1} and dH represents the minimum height of the raining column in km.

2.2 Rainfall retrieval from TRMM precipitation radar

The TRMM satellite is a polar satellite that flies at an altitude of about 400 km and covers a latitudinal band between ∼37° S and ∼37° N. The onboard precipitation radar (PR) is the first active precipitation measuring instrument launched into space. The PR obtains information on precipitation at a vertical and horizontal (nadir) resolutions of 250 m and 4.3 km, respectively. More details on the TRMM satellite and its instrument configuration can be found in Kummerow et al. (1998).

Since the PR suffers from considerable attenuation by large rain droplets, a correction algorithm has been developed and applied to the measured radar echo intensities (Z). Subsequently, the corrected radar echo intensities are converted into rainfall rates (R), using separate droplet size distributions for stratiform and convective precipitation, which are composed of Z–R relations measured during aircraft campaigns at various locations around the world (Iguchi et al., 2000). In this research, we use the near-surface observed precipitation from the TRMM PR 2A25 (version 5) product. This product has been validated over West Africa using rain gauge measurements for the 1998 monsoon season (Nicholson et al., 2003) and over Florida using ground-based rain radar (Liao and Meneghini, 2009). In the former study, it was found that the seasonally averaged bias of TRMM-PR is +0.3 mm d^{-1} (+7% relative), with an RMSE of 1.9 mm d^{-1}. In the latter study, a TRMM-PR overestimate for stratiform rain by 9% was

HESSD
7, 6351–6380, 2010

revealed, whereas convective rainfall is underestimated by 19%.

2.3 Evaluation of SEVIRI rain rates

2.3.1 Comparison with TRMM-PR

As mentioned earlier, this paper first presents an evaluation of the CPP-PP algorithm over West Africa using TRMM-PR observations by comparing 1) the observed areal rainfall and instantaneous rain rates of SEVIRI and TRMM-PR and 2) the SEVIRI- and TRMM-PR-observed frequency distributions of rain rate. Both comparisons have been performed for the region 20° S–20° N, 20° W–20° E for May and June 2006.

Initially, 150 TRMM-PR overpasses were selected and collocated with the SEVIRI rainfall retrievals. Both SEVIRI and TRMM-PR retrievals have been reprojected to a common 0.1°×0.1° grid (∼11×11 km). A sensitivity analysis has revealed that results do not change significantly when the grid size is doubled.

For each TRMM-PR overpass, the SEVIRI image closest in time was selected, which gives a maximum time difference between SEVIRI and TRMM observations of ∼7 min. An example of a collocated TRMM-PR overpass with SEVIRI is shown in Fig. 1. In order to avoid possible spatial collocation mismatches, we refrained from comparing pixel-by-pixel values. Instead, we calculated the mean rainfall area and the median rain rate. The TRMM-PR and CPP-PP areal rainfall has been calculated by dividing the number of grid boxes for which TRMM-PR-observed rain rate exceeded the 0.5 mm h^{-1} detection threshold (Liao and Meneghini, 2009) to the total number of grid boxes in a TRMM-PR overpass. In 23 overpasses, no rain was detected, so 127 TRMM-PR overpasses were included in the comparison dataset.

Additional to the comparison of SEVIRI- and TRMM-PR-derived rain rates per overpass, the relative and cumulative frequency distributions were computed for the aggregated overpasses. A bootstrapping technique was applied to obtain an indication on the uncertainty of the obtained cumulative distribution functions. Using this bootstrapping technique, from the total number of about 14 000 pixels 10 000 new cumulative frequency distributions were computed by randomly drawing values from the original observations.

2.3.2 Comparison with rain gauge observations

Rain gauge observations from 16 stations of the African monsoon multidisciplinary analysis project (AMMA, Redelsperger et al., 2006) were used as a second evaluation dataset. Since satellite and ground-based rainfall observations are difficult to compare in terms of time series or on a pixel-to-pixel basis (areal averages observed from satellite versus point measurements from rain gauges), the rain gauge observations were only included in the comparison of the relative and cumulative frequency distributions. The 16 observation stations were located near Niamey, Niger (13.5° N, 2.1° E, 8 stations) and Nangatchouri, Benin (9.7° N, 1.6° E, 8 stations). Precipitation was recorded at a 5-min resolution, which was aggregated to 15-min resolution to correspond with the SEVIRI observation times. Since the CPP-PP algorithm only retrieves precipitation during daylight hours, we only analyzed daytime observations between 07:30 and 16:30 UTC (LT). To obtain a substantial statistical dataset, rain gauge observations for the 16 stations over the period May–September for 2005, 2006, and 2007 were collected.

2.4 Evaluation of the monsoon progression over West Africa

In addition to the verification of the accuracy of the CPP-PP retrievals of rainfall area and rain rate, the detection of the WAM rainfall progression on a seasonal and synoptical scale is of interest. To investigate this ability for CPP-PP, latitudinal and longitudinal Hovmüller diagrams were constructed for rain occurrence frequency and rain rate over the period May–September 2006. In this period, two data gaps in our SEVIRI data archive occurred (1–7 August and 24–30 September), but still nearly 90% of the total number of daytime observations were available. Latitudinal Hovmüller diagrams were constructed for 0°–20° N, with values integrated over 10° W–10° E, whereas the longitudinal diagrams were calculated between 12° W–20° E, with values integrated over 7°–20° N, thereby only including retrievals over the West African continent.

The daytime diurnal cycle of precipitation was investigated for three areas. The latitudinal bands were chosen analogously to Mohr (2004), which were primarily based on vegetation type: 7°–10° N (rain forest), 10°–15° N (savannah), and 15°–20° N (semi-desert). Within these areas, for May–September 2006 all 15-min CPP-PP retrievals with R>0.5 mm h^{-1} were collected into 1-h bins (centered at 08:00, 09:00, ..., 15:00, 16:00 LT). Subsequently, for each hour the 25th, 50th, 75th, and 90th percentiles of rain rate were calculated.

Finally, the longitudinal Hovmüller diagrams were constructed to demonstrate that SEVIRI daytime precipitation retrievals can be used to monitor the monsoon progression at a synoptical scale. We selected 163 daytime MCSs by visual inspection of the Hovmüller diagrams. Convective systems with durations less than 2 h or systems being initiated after 15:30 LT were not included in the dataset. For each day, the westward travel speed and relative contribution of MCSs to the total rainfall amount were calculated. The MCS travel speed was calculated by dividing the traversed westward distance by the amount of hours that the MCS was visible in the longitudinal Hovmüller diagram. Subsequently, the precipitation produced by MCSs was calculated through integration of the rain rates within the contour lines pertaining to the MCS and the ratio of MCS to the total daytime precipitation was calculated.

3 Results

3.1 Validation of SEVIRI rainfall retrievals with TRMM-PR

Figure 2 presents the obtained rainfall area and median rain rate per TRMM-PR overpass from SEVIRI and TRMM-PR data. The left panel in Fig. 2 shows that the TRMM-PR and CPP-PP rainfall area agree well (corr=0.86). However, the rainfall area retrieved by CPP-PP is about 10% larger than the area observed by TRMM-PR. This

HESSD
7, 6351–6380, 2010

difference might be a result from differences in the rainfall observation techniques of TRMM-PR and SEVIRI, or the threshold settings used to separate precipitating from non-precipitating pixels.

The scatter plot of median rain rate per TRMM-PR overpass (Fig. 2, right panel) reveals that the correlation between TRMM-PR and SEVIRI is weaker than for rainfall area. Also, the dynamic range of 0–3 mm h^{-1} for TRMM-PR is about 75% smaller than for SEVIRI (0–5 mm h^{-1}). As noted earlier, Liao and Meneghini (2009) found that TRMM-PR retrieves lower rain rates for convective systems as compared to ground-based radar observations.

The cumulative and relative frequency distributions are presented in Fig. 3. The shaded areas indicate the respective standard deviations of the cumulative frequency per rain rate bin, which were calculated using the bootstrapping technique. For low rain rates, SEVIRI underestimates the frequency relative to TRMM-PR. However, rain rates >~7 mm h^{-1} are more frequently retrieved by the CPP-PP algorithm. Furthermore, between 7 and 10 mm h^{-1} the SEVIRI and TRMM-PR cumulative frequency distributions are significantly different, which follows from the non-overlapping standard deviations in Fig. 3. The more frequent retrievals of the higher rain rates by CPP-PP from SEVIRI gradually translate into a difference between the SEVIRI and TRMM-PR cumulative frequency distributions. For example, the median TRMM-PR and CPP-PP values are similar, but at the 75th percentile the CPP-RR value is 1.7 mm h^{-1} higher than TRMM-PR.

Also shown in Fig. 3 are results for the aggregated rain gauge data. Interestingly, both TRMM-PR and SEVIRI have larger values than the rain gauges throughout almost the entire cumulative frequency distribution. Despite that 16 rain gauges were used to compose the distribution functions, a proper comparison of point measurements from gauges to the areal rainfall estimates from satellites is a complex process, which necessitates substantial corrections to the gauge observations (Flitcroft et al., 1989). Especially over West Africa, a large anisotropy in rainfall variability due to the steep north–south gradient exists. Relative errors in rain gauge observations for the Sahel

HESSD
7, 6351–6380, 2010

zone are large due to the large intermittent nature of rainfall in this region (Ali et al., 2005b,a).

3.2 Monitoring of daylight time monsoon progression for 2006

The 2006 monsoon season was a near-normal season in terms of rainfall amount (Janicot et al., 2008). However, in June some excessive rainfall events around 15° N occurred, which decreased the generally strong north–south rainfall gradient. Further, the monsoon was fully established around 10 July, which is about 15 days later than the climatological average found by Sultan and Janicot (2003) (Janicot et al., 2008). The late monsoon arrival in 2006 was among others connected to warmer sea surface temperatures (SST) in the Guinean Gulf, which decreased the land-sea temperature gradient and hence weakened the advection of moisture by the monsoon winds.

Figure S1 shows for our daytime retrievals the evolution of monthly mean rain occurrence, median rain rate, and median daytime rainfall over West Africa throughout the monsoon season. In May, the major convective activity can be found over the oceanic area south of 7° N. Some early convective activity is also found over the continent around 13° N, the median rain rates are generally lower than 0.25 mm h^{1}, and the mean daytime rainfall totals hardly exceed 1 mm d^{-1}. In June, the area around 15° N is of particular interest. In this area the median rain rates are high (>1 mm h^{-1}) while the mean rain occurrence frequencies are low (<10%). More detailed analysis revealed that a few excessive early monsoon thunderstorms produced most rainfall in this area (see also Janicot et al., 2008). Guichard et al. (2009) suggested that these thunderstorms culminated from an increase in specific humidity, precipitable water, and equivalent potential temperature (a metric for low-level moist static energy) which occur from May onwards in this region. Opposite behavior is observed in the area along the Guinean coast round 5° N where the mean rain occurrence frequencies are high (>40%) and the median rain rates are low (<0.5 mm h^{-1}). In July, the areas with the highest rain occurrence frequencies shift from about 10° to 13° N. Rain rates further increase north of 15° N, which results in an increase of the daytime rain totals compared to June. The median daytime rainfall values remain high along the Eastern Guinean coast, which is a compensation effect of a high rain occurrence frequency and low rain rates.

In August, the highest rain occurrence is found between 10° N and 15° N. However, it is rather due to the high rain occurrence than due to a high rain rate that daytime rainfall values remain relatively high (>1.5 mm d^{-1}). In contrast, the patches of high daytime rainfall that occur over the region north of 15° N and east of 4° E are caused by a few intensive rain events, which might be initiated through interaction of AEWs with the Aïr mountains located near 17° N, 8° E. The gradual retreat of the ITCZ is visible in September as a decrease in rain occurrence and daytime rainfall for the region north of 10° N. On the other hand, south of 10° N rain occurrence and rain rate slightly increase again.

A more detailed picture of the rainfall activity throughout the 2006 monsoon season for 0°–20° N is given in the latitudinal Hovmüller plots in Fig. 4. During the second part of May and first days of June some early convective activity is seen. In June, the main rainy areas are concentrated in the coastal region around 7° N and convection is inhibited over the continent, except for the earlier mentioned convective activity around 15° N. It was suggested by Janicot et al. (2008) that the decrease in convection was caused by a weaker TEJ (TEJ) and a Kelvin wave pattern that moved from South-America to Africa and triggered upper-air convergence. In addition, the warmer than normal SST in the Guinean Gulf may have further decreased advection of moist oceanic air to the continent (weaker sea breeze pattern).

Convection over the continent remains suppressed until around mid-July, at which the well-known "monsoon jump" occurs. This jump corresponds fairly well with the reported date of 10 July by Janicot et al. (2008). From that date onwards until mid-August, the major convective bands are located between 10° and 15° N, as can be seen from the rain rate plot. Finally, towards September, the monsoon rains gradually retreat southward which can be seen from the diminishing rain occurrence frequency.

HESSD
7, 6351–6380, 2010

Figure 5 shows the daylight diurnal cycle of rain rate and rain occurrence for three regions: 7°–10° N, 10°–15° N, and 15°–20° N, with all areas having longitudinal extents 10° W–10° E. For convenience, the regions are designated as rain forest, savannah, and semi-desert, respectively, consistent with the analysis of Mohr (2004). To reduce noise in the results, only rain rates larger than 0.5 mm h^{-1} were included.

Over the rain forest region (7°–10° N), the median rain rate decreases during morning and early afternoon and increases in the late afternoon in May and June. It was shown by Mohr et al. (2003) that over rain forest convection becomes shallower than over savannah and semi-desert due to a moister boundary layer resulting from evapotransiration. The daytime median rainfall reduces further during July, from about 4 to 2 mm h^{-1}. The rain occurrence remains rather constant throughout the day at about 4%. Also during August, rain occurrence frequency remains constant, and the median rain rate does not exceed 3 mm h^{-1}. In connection with Fig. S1, it can be concluded that the rain forest region is located southward of the heavy monsoon rains. In September, strong increased rain occurrence leads to a marginal increase in the amount of precipitation. Thus it can be concluded that the rain forest region is located south of the heavy monsoon rains.

The savannah region (10°–15° N) shows an increase in rain occurrence frequency and rain rate during the afternoon in May (from 1.5–3 mm h^{-1}), which is probably related to convection initiated by differential heating of the surface. This type of convection is typical for tropical regions outside monsoon areas and has been documented by e.g., Nesbitt and Zipser (2003), Mohr (2004), and Singh and Nakamura (2010). The afternoon increase is still visible in June (from ~3–5 mm h^{-1}), but in July and August the monsoon rains show a small daytime diurnal cycle. The rain occurrence frequency increases from 3–5% in May and June towards 10% in August. Similar to the rain forest region, rain rates decrease during daytime from 6 to 3 mm h^{-1}. This decrease in rainfall is tied with a decrease in the CWP diurnal cycle, as noted by Greuell et al. (2010). The decrease in CWP and rainfall may be related to a typical diurnal cycle of MCSs with a maximum during nighttime. MCSs in the ITCZ are dynamically forced through

HESSD
7, 6351–6380, 2010

Rainfall monitoring West-Africa with SEVIRI

E. L. A. Wolters et al.

the AEWs and show less dissipation during nighttime. In addition, they are maintained through infrared cooling at the top (Dai, 2001; Yang and Smith, 2006).

For the semi-desert area (15°–20° N), the rain occurrence in May and June is lower than for the other two regions. A clear signal of late afternoon convection (triggered by differential heating) is seen for these months, with the most pronounced increase in rain rate during the afternoon in June (from 1–7 mm h^{-1}). Simultaneous with the increase in rain rate, the rain occurrence frequency also sharply increases during the afternoon in June. From July to August the monsoon rains move over the semi-desert region; rain rate and rain occurrence frequency show virtually no development during the daytime period. The mean rain occurrence frequency increases from ∼1% to ∼3% between July and August, which suggests that the real monsoon rains started in August in this region. As the ITCZ reaches its northernmost location in this region in August, it is not surprising that for September the daytime rainfall signal becomes similar to the pre-monsoon months. Again, there is very little rain occurrence (<0.5%) during the morning, but as the day progresses convection is triggered due to increased instability. The median rain rate increases from 1 mm h^{-1} to 8 mm h^{-1} between 10 and 16 UTC.

Figure S2 presents longitudinal Hovmüller diagrams of rain occurrence and rain rate for May–September 2006 for 7°–20° N, 12° W–20° E over land surfaces. Since MCSs are transported through AEWs, these diagrams can provide information on position and longitudinal travel speed longitudes of MCSs. Please note that as a result of using daytime only data, no clear distinction between prevailed initiation and maintenance of MCSs can be made. The westward motion of the MCSs can clearly be deduced from the slope of the contour shadings in Fig. S2.

Figure 6 presents the number and monthly mean westward travel speed of the MCSs counted in the area evaluated in Fig. S2. It is noted that both in August and September no SEVIRI data were available in our archive for 7 days, which impacts the number of detected MCSs for these months. The mean MCSs travel speed is ∼53 km h^{-1} for May and June, followed by a small increase in July. This increase is likely connected to a strengthening of the African Easterly Jet in combination with its axis moving over

HESSD

7, 6351–6380, 2010

the West African continent (Janicot et al., 2008). In August and September, the travel speed fluctuates between 40 and 50 km h^{-1}.

Figure 7 shows the ratio of MCS-produced rainfall to the total amount of rainfall for the area evaluated in Fig. S2. The ratio of MCS precipitation to the total daytime precipitation shows a drop from 30–35% in May and June to 20% in July. It is suggested that the drop in precipitation ratio is connected to the more frequent non-convective rain over the rain forest area or from more precipitation fallen from the remnants of nighttime MCSs. In addition, in May and June the amount of MCSs is larger than in July. In September the ratio increases again to 26%, but remains below the values of May and June. The average over May–September 2006 is 27%, which is closer to the estimate of Laing et al. (1999) than that of Mathon et al. (2002). It should be noted that our estimate is based on visual inspection of the Hovmüller diagrams and no tracking algorithm has been used. Convective systems with a duration less than two hours have been excluded. In spite of this, ratio estimates from a more sophisticated method would most likely be close to the estimate of Laing et al. (1999) of about 22%. The 90% found by Mathon et al. (2002) was obtained for a limited area (16 000 km^2) over the Sahel region, which is a region with both low total rainfall and a large interannual variation in total rainfall and is largely dependent on the precipitation provided by large organized systems.

4 Summary and conclusions

This paper presents the application of the CPP-PP rain retrieval algorithm on SEVIRI visible and near-infrared reflectances over West Africa for May through September 2006. The algorithm combines retrieved cloud particle effective radius, cloud phase, and cloud-top temperature information to estimate the rain rate. Instantaneous rain retrievals were compared against TRMM-PR and rain gauge observations. CPP-PP is well able to capture the rainfall characteristics observed by TRMM-PR; the areal rainfall retrieved by CPP-PP of 2.5% is higher than the corresponding value from TRMM-PR of

2.0%, which is a satisfactory comparison given the different measurement techniques. Further, it was shown that the mean retrieved rain rate from CPP-PP is ≈8% higher than from TRMM-PR and that the dynamic range of the CPP-PP retrieved rain rates is about 75% larger than for TRMM-PR. The frequency distributions of TRMM-PR and CPP-PP are similar until their median values, but beyond this value CPP-PP retrieves higher rain rates than TRMM-PR. Although TRMM-PR is the state-of-the-art instrument for retrieving rainfall over the tropics, there are known biases, such as an underestimation of rain rates in heavier convective systems (Liao and Meneghini, 2009). On the other hand, CPP-PP on SEVIRI may retrieve too high rain rates, especially in the tropics, due to the fact that a considerable amount of the precipitation at cloud base may evaporate. The fraction of evaporation below the cloud base may add up to 50%, depending on cloud base height, rain rate at cloud base, and the below-cloud relative humidity (Rosenfeld and Mintz, 1988). A simple parameterization to correct for the below-cloud evaporation will be implemented in CPP-PP in the near future.

A second goal of this paper was to demonstrate to which extent the CPP-PP rain retrievals can be used to monitor the progression of the West African monsoon. Using Hovmüller diagrams in both latitudinal and longitudinal directions, it was shown that this progression can be followed on both seasonal and synoptical time scales. The unprecented 15-min temporal resolution in combination with the $3\times3\,\text{km}^2$ spatial resolution of the SEVIRI instrument makes this the best suited instrument for monitoring the movement of convective systems throughout the monsoon season, despite the limitation to daytime data. Through visual inspection of the longitudinal Hovmüller diagrams, which were constructed for the West African continent, a selection of MCSs was made and their westward travel speed and contribution to the total amount of rainfall was calculated. The travel speed increases from roughly $50\,\text{km}\,\text{h}^{-1}$ in May and June to $61\,\text{km}\,\text{h}^{-1}$ in July, after which it decreases again to $40\text{–}50\,\text{km}\,\text{h}^{-1}$ in August and September. It was suggested that the increase in July is connected to a stronger AEJ in July in combination with its location over the West African continent. The monthly mean ratio of MCS precipitation to the daytime total amount varies from 22–35%, with

HESSD
7, 6351–6380, 2010

a mean of 27% over the five months investigated. This estimate is close to the 22% found by Laing et al. (1999).

The use of retrieved cloud-top properties from SEVIRI to estimate rain rates is a much more physically based principle than the widely used cold cloud duration techniques developed in the 1970s and 1980s. Despite the disadvantage of only having retrievals during daytime, the high temporal and spatial resolution of SEVIRI more than compensates for this. Over West Africa, about 40 rain retrievals per day can be made available for a single location. In contrast, the TRMM satellite revisits the same location only once in ~10 days and the full diurnal cycle is captured once every 47 days, which necessitates at least several years of data to obtain substantial statistical datasets. Being operational since 2004, SEVIRI enables a longterm climatology on rainfall characteristics over West Africa and the relation to land surface properties. These climatological quantities might be useful to evaluate the cloud and rainfall parameterization of regional climate models. In addition, monitoring the travel speed, size and duration of large convective systems may als be beneficial to other purposes, such as e.g. more accurate monitoring of potential Atlantic hurricanes.

Supplementary material related to this article is available online at: http://www.hydrol-earth-syst-sci-discuss.net/7/6351/2010/hessd-7-6351-2010-supplement.zip.

Acknowledgements. This research was carried out within the Water Cycle Multi Mission Observation Strategy (WACMOS) project of the European Space Agency (ESA). TRMM-PR data was downloaded from the DAAC Data Pool at NASA Goddard Space and Flight Center (GSFC). The authors thank Jan Fokke Meirink (KNMI) for his useful comments to improve the manuscript. Finally, we acknowledge Theo Vischel (Laboratoire d'étude des Transferts en Hydrologie et Environnement, LTHE, Grenoble, France) and Luc Le Barbé (L'Institut de Recherche pour le Développement, IRD Benin) for providing the AMMA rain gauge data.

HESSD

7, 6351–6380, 2010

Rainfall monitoring West-Africa with SEVIRI

E. L. A. Wolters et al.

References

Adler, R. F. and Negri, A. J.: Satellite infrared technique to estimate tropical convective and stratiform rainfall, J. Appl. Meteorol., 27, 30–71, 1988. 6353

Ali, A., Amani, A., Diedhiou, A., and Lebel, T.: Rainfall estimation in the Sahel. Part II: Evaluation of rain gauge networks in the CILSS countries and objective intercomparison of rainfall products, J. Appl. Meteorol., 44, 1707–1722, doi:10.1175/JAM2305.1, 2005a. 6363

Ali, A., Lebel, T., and Amani, A.: Rainfall Estimation in the Sahel. Part I: Error function., J. Appl. Meteorol., 44, 1691–1706, doi:10.1175/JAM2304.1, 2005b. 6353, 6363

Ba, M. B. and Gruber, A.: GOES multispectral rainfall algorithm (GMSRA), J. Appl. Meteorol., 40, 1500–1514, 2001. 6353

Basu, B. K.: Diurnal variation in precipitation over India during the summer monsoon season: observed and model predicted, Mon. Weather Rev., 135, 2155–2167, doi:10.1175/MWR3355.1, 2007. 6355

Da, A.: Global precipitation and thunderstorm frequencies. Part II: Diurnal variations., J. Climate, 14, 1112–1128, doi:10.1175/1520-0442(2001)014<1112:GPATFP>2.0.CO;2, 2001. 6366

De Haan, J. F., Bosma, P. B., and Hovenier, J. W.: The adding method for multiple scattering calculations of polarized light, Astron. Astrophys., 183, 371–391, 1987. 6357

Flitcroft, I. D., Milford, J. R., and Dugdale, G.: Relating point to area average rainfall in semiarid West Africa and the implications for rainfall estimates derived from satellite data, J. Appl. Meteorol., 28, 252–266, doi:10.1175/1520-0450(1989)028<0252:RPTAAR>2.0.CO;2, 1989. 6362

Greuell, J. W., van Meijgaard, E., and Clerbaux, N.: Evaluation of model predicted top-of-atmosphere radiation and cloud parameters over Africa with observations from GERB and SEVIRI, J. Climate, submitted, 2010. 6365

Guichard, F., Kergoat, L., Mougin, E., Timouk, F., Baup, F., Hiernaux, P., and Lavenu, F.: Surface thermodynamics and radiative budget in the Sahelian Gourma: seasonal and diurnal cycles, 375, 161–177, doi:10.1016/j.jhydrol.2008.09.007, 2009. 6363

Iguchi, T., Kozu, T., Meneghini, R., Awaka, J., and Okamoto, K.: Rain profiling algorithm for TRMM precipitation radar data, J. Appl. Meteorol., 39, 2038–2052, 2000. 6358

Janicot, S., Thorncroft, C. D., Ali, A., Asencio, N., Berry, G., Bock, O., Bourles, B., Caniaux, G., Chauvin, F., Deme, A., Kergoat, L., Lafore, J.-P., Lavaysse, C., Lebel, T., Marticorena, B., Mounier, F., Nedelec, P., Redelsperger, J.-L., Ravegnani, F., Reeves, C. E., Roca, R., de Rosnay, P., Schlager, H., Sultan, B., Tomasini, M., Ulanovsky, A., and ACMAD forecasters team: Large-scale overview of the summer monsoon over West Africa during the AMMA field experiment in 2006, Ann. Geophys., 26, 2569–2595, doi:10.5194/angeo-26-2569-2008, 2008. 6363, 6364, 6367

Kidd, C.: Satellite rainfall climatology: a review, Int. J. Climatol., 21, 1041–1066, doi:10.1002/joc.365, 2001. 6354

Kummerow, C., Barnes, W., Kozu, T., Shuie, J., and Simpson, J.: The Tropical Rainfall Measuring Mission (TRMM) sensor package, J. Atmos. Ocean. Technol., 15, 809–817, 1998. 6358

Laing, A. G., Fritsch, J. M., and Negri, A. J.: Contribution of mesoscale convective complexes to rainfall in Sahelian Africa: estimates from geostationary infrared and passive microwave data, J. Appl. Meteorol., 38, 957–964, doi:10.1175/1520-0450(1999)038<0957:COMCCT>2.0.CO;2, 1999. 6354, 6367, 6369

Liao, L. and Meneghini, R.: Validation of TRMM precipitation radar through comparison of its multiyear measurements with ground-based radar, J. Appl. Meteorol. Clim., 48, 804–817, 2009. 6358, 6359, 6362, 6368

Mathon, V., Laurent, H., and Lebel, T.: Mesoscale convective system rainfall in the Sahel, J. Appl. Meteorol., 41, 1081–1092, 2002. 6354, 6367

Mecikalsi, J. R. and Bedka, K. M.: Forecasting convective initiation by monitoring the evolution of moving cumulus in daytime GOES imagery, Mon. Weather Rev., 134, 49–78, 2006. 6353

Mohr, K. I.: Interannual, monthly, and regional variability in the west season diurnal cycle of precipitation in Sub-Saharan Africa, J. Climate, 17, 2441–2453, 2004. 6361, 6365

Mohr, K. I., Baker, R. D., Tao, W. K., and Famiglietti, J. S.: The sensitivity of West African convective line water budgets to land cover, J. Hydrometeorol., 4, 62–76, 2003. 6365

Negri, A. J. and Adler, R. F.: An intercomparison of three satellite infrared rainfall techniques over Japan and surrounding waters, J. Appl. Meteorol., 32, 357–373, 1993. 6353

Negri, A. J., Adler, R. F., and Wetzel, P. J.: Satellite rain estimation: An analysis of the Griffith-Woodley technique, J. Clim. Appl. Meteorol., 26, 1565–1576, 1984. 6353

Nesbitt, S. W. and Zipser, E. J.: The diurnal cycle of rainfall and convective intensity according to three years of TRMM measurements, J. Climate, 16, 1456–1475, 2003. 6365

Nicholson, S. E., Tucker, C. J., and Ba, M. B.: Desertification, drought, and surface vegetation: an example from the West African Sahel, B. Am. Meteorol. Soc., 79, 815–829, 1998. 6354

HESSD

7, 6351–6380, 2010

Rainfall monitoring West-Africa with SEVIRI

E. L. A. Wolters et al.

Nicholson, S. E., Some, B., McCollum, J., Nelkin, E., Klotter, D., Berte, Y., Diallo, B. M., Gaye, I., Kpabeba, G., Ndiaye, O., Noukpozounkou, J. N., Tanu, M. M., Thiam, A., Toure, A. A., and Traore, A. K.: Validation of TRMM and other rainfall estimates with a high-density gauge dataset for West Africa. Part II: Validation of TRMM rainfall products, J. Appl. Meteorol., 42, 1355–1368, doi:10.1175/1520-0450(2003)042<1355:VOTAOR>2.0.CO;2, 2003. 6358

Pruppacher, H. R. and Klett, J. D.: Microphysics of Clouds and Precipitation, 2nd rev. and enl. ed., Kluwer Academic Publishers, Dordrecht, The Netherlands, 1997. 6353

Ramel, R., Gallée, H., and Messager, C.: On the northward shift of the West African monsoon, Clim. Dynam., 26, 429–440, doi:10.1007/s00382-005-0093-5, 2006. 6355

Redelsperger, J., Thorncroft, C. D., Diedhiou, A., Lebel, T., Parker, D. J., and Polcher, J.: African monsoon multidisciplinary analysis: an international research project and field campaign, B. Am. Meteorol. Soc., 87, 1739–1746, doi:10.1175/BAMS-87-12-1739, 2006. 6360

Roebeling, R. A. and Holleman, I.: Validation of rain rate retrievals from SEVIRI using weather radar observations, J. Geophys. Res., 114, doi:10.1029/2009JD012102, 2009. 6355, 6356, 6357

Roebeling, R. A., Feijt, A. J., and Stammes, P.: Cloud property retrievals for climate monitoring: implications of differences between Spinning Enhanced Visible and Infrared Imager (SEVIRI) on Meteosat-8 and Advanced very high resolution radiometer (AVHRR) on NOAA-17, J. Geophys. Res., 111, doi:10.1029/2005JD006990, D20210, 2006. 6356

Rosenfeld, D. and Mintz, Y.: Evaporation of rain falling from convective clouds as derived from radar measurements, J. Appl. Meteorol., 27, 209–215, doi:10.1175/1520-0450(1988)027<0209:EORFFC>2.0.CO;2, 1988. 6368

Singh, P. and Nakamura, K.: Diurnal variation in summer monsoon precipitation during active and break periods over Central India and Southern Himalayan Foothills, J. Geophys. Res., 115, D12122, doi:doi:10.1029/2009JD012794, 2010. 6365

Stammes, P.: Spectral radiance modelling in the UV-visible range, in: IRS 2000: Current Problems in Atmospheric Radiation, edited by: Smith, W. L. and Timofeyev, Y. M., A. Deepak, Hampton, VA, 385–388, 2001. 6357

Sultan, B. and Janicot, S.: The West African monsoon dynamics. Part II: The "preonset" and "onset" of the summer monsoon, J. Climate, 16, 3407–3427, doi:10.1175/1520-0442(2003)016<3407:TWAMDP>2.0.CO;2, 2003. 6354, 6355, 6363

Sultan, B., Janicot, S., and Drobinski, P.: Characterization of the diurnal cycle of the West African monsoon around the monsoon onset, J. Climate, 20, 4014–4032, doi:10.1175/

JCLI4218.1, 2007. 6355
Taylor, C. M. and Ellis, R. J.: Satellite detection of soil moisture impacts on convection at the mesoscale, Geophys. Res. Lett., 33, doi:10.1029/2005GL025252, 2006. 6355
Taylor, C. M., Parker, D. J., and Harris, P. P.: An observational case study of mesoscale atmospheric circulations induced by soil moisture, Geophys. Res. Lett., 34, L15801, doi:10.1029/2007GL030572, 2007. 6355
Wentz, F. J. and Spencer, R. W.: SSM/I rain retrievals within a unified all-weather ocean algorithm, J. Atmos. Sci., 55, 1613–1627, 1998. 6356
Wolters, E. L. A., Roebeling, R. A., and Feijt, A. J.: Evaluation of cloud phase retrieval methods for SEVIRI onboard Meteosat-8 using ground-based lidar and cloud radar data, J. Geophys. Res., 47, 1723–1738, doi:10.1175/2007JAMC1591.1, 2008. 6357
Wolters, E. L. A., Deneke, H. M., van den Hurk, B. J. J. M., Meirink, J. F., and Roebeling, R. A.: Broken and inhomogeneous cloud impact on satellite cloud particle effective radius and cloud-phase retrievals, J. Geophys. Res., 115, D10214, doi:10.1029/2009JD012205, 2010. 6357
Yang, S. and Smith, E. A.: Mechanisms for diurnal variability of global tropical rainfall observed from TRMM, J. Climate, 19, 5190–5226, doi:10.1175/JCLI3883.1, 2006. 6366
Zinner, T., Mannstein, H., and Tafferner, A.: Cb-TRAM: Tracking and monitoring severe convection from onset over rapid development to mature phase using multi-channel Meteosat-8 SEVIRI data, Meteorol. Atmos. Phys., 101, 191–210, doi:10.1007/s00703-008-0290-y, 2008. 6353

HESSD
7, 6351–6380, 2010

Rainfall monitoring West-Africa with SEVIRI

E. L. A. Wolters et al.

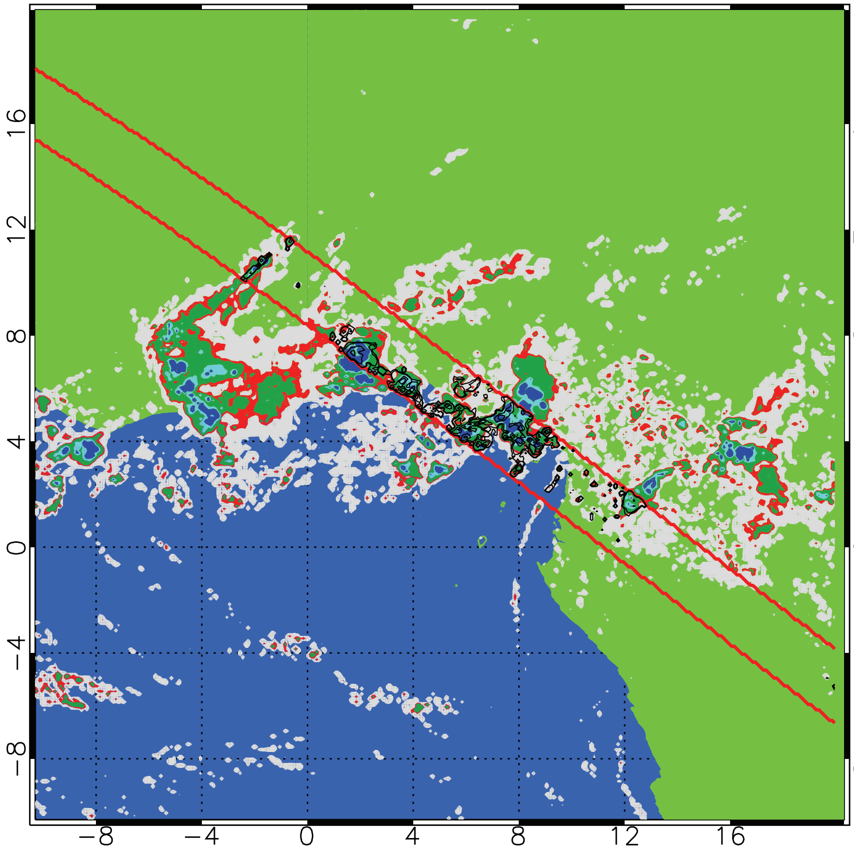

Fig. 1. Example of a collocated SEVIRI image with a TRMM-PR overpass over the Guinean coastal area for 16 May 2006, 11:15 UTC. SEVIRI rain rates are in color-filled contours, while TRMM-PR rain rates are indicated by open contours. Countour intervals are drawn at 0.1, 0.5, 1, 5, and 10 mm h^{-1}. The red lines indicate the edges of the TRMM-PR swath.

HESSD
7, 6351–6380, 2010

Rainfall monitoring West-Africa with SEVIRI

E. L. A. Wolters et al.

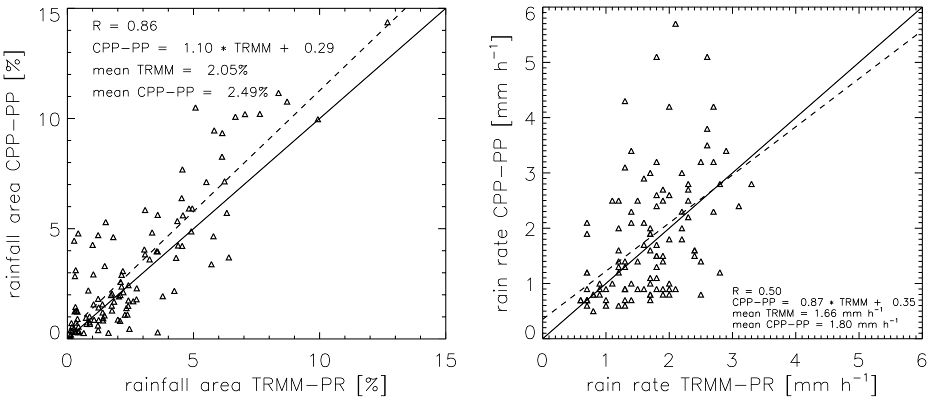

Fig. 2. (Left) detected rainfall area (in % per TRMM-PR overpass) for clouds with $R>0.5\,\mathrm{mm\,h^{-1}}$ and (right) the corresponding median rain rates per overpass as observed by TRMM-PR and SEVIRI. Solid lines indicate the 1:1 relation, dashed lines denote linear regressions.

HESSD
7, 6351–6380, 2010

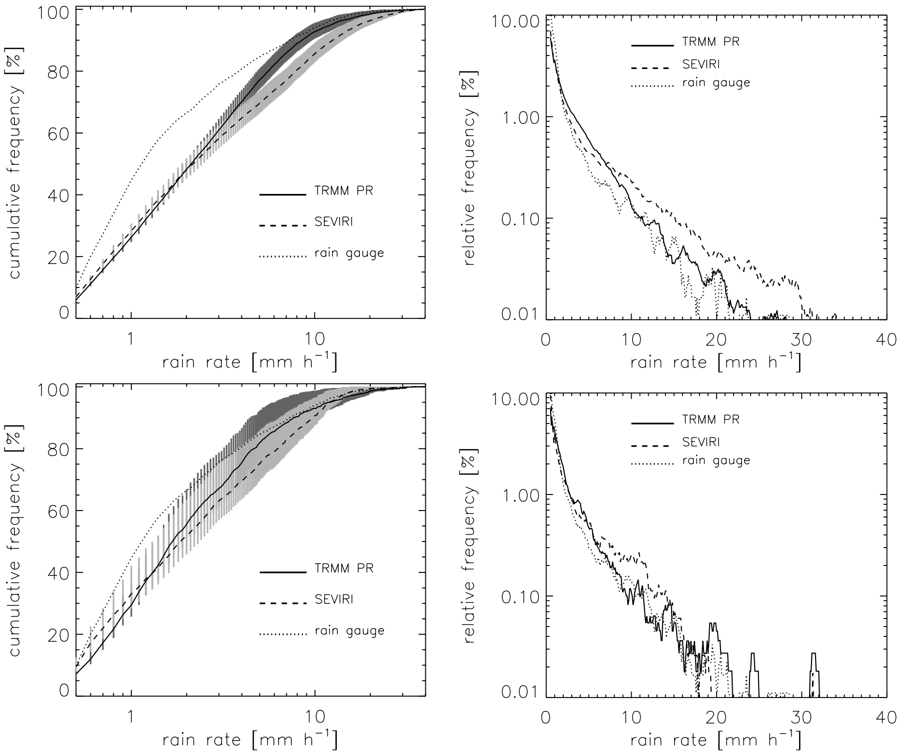

Fig. 3. (Left) cumulative frequency distribution of rain rate derived from (solid) TRMM-PR, (dashed) SEVIRI using CPP-PP, and (dotted) daytime (07:30–16:30 LT) rain gauge observations. Note the logarithmic scaling on the x-axis. The superimposed grey scales for TRMM-PR and SEVIRI denote the standard deviation at each rain rate bin, which was obtained from a bootstrapping technique using 10 000 draws. (Right) corresponding relative frequency distribution for TRMM-PR, SEVIRI, and rain gauge with logarithmic scaling on the y-axis. Results are shown for for (top) 20° W–20° E, 20° S–20° N and (bottom) 1°–3° E, 9°–14° N.

HESSD
7, 6351–6380, 2010

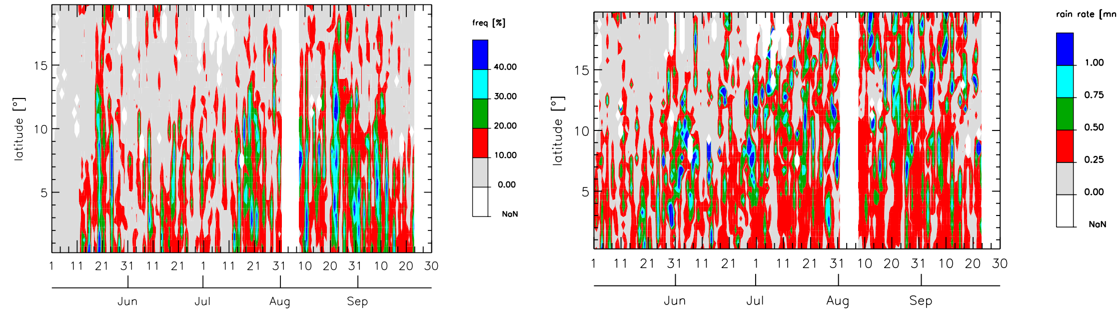

Fig. 4. Latitudinal Hovmüller diagrams for (top) daytime rain frequency and (bottom) mean daytime conditional rain rate ($R>0\,\mathrm{mm\,h^{-1}}$) for 0°–20° N. Values have been obtained over 10° W–10° E.

HESSD
7, 6351–6380, 2010

Rainfall monitoring West-Africa with SEVIRI

E. L. A. Wolters et al.

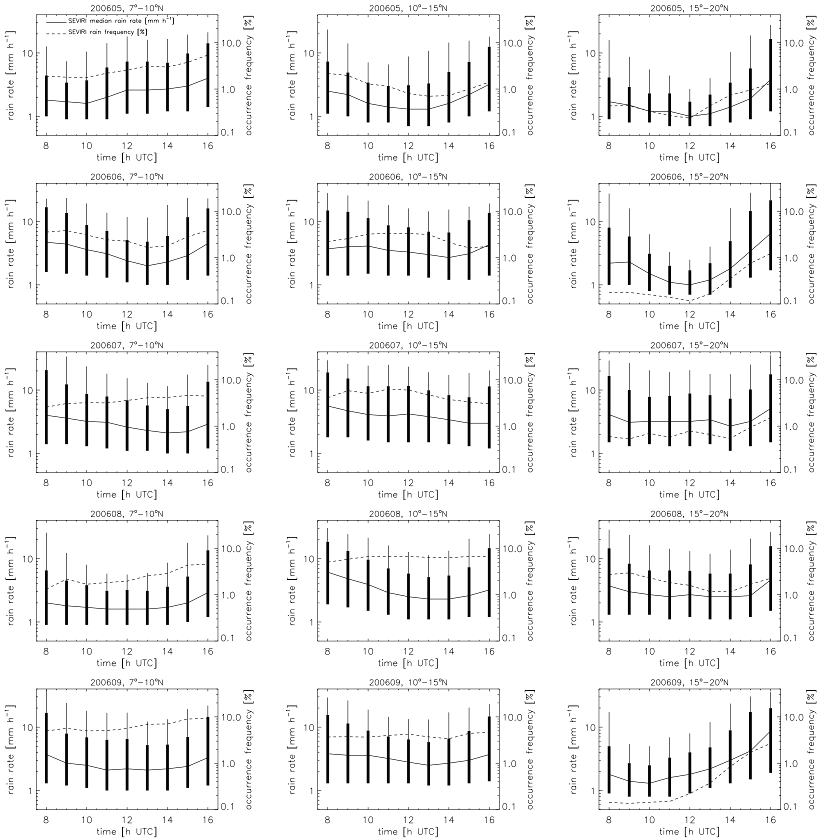

Fig. 5. Daylight time cycle of precipitation from May through September 2006 for (left column) 7°–10° N, (middle column) 10°–15° N, and (right column) 15°–20° N. CPP-PP rain retrievals with R>0.5 mm h^{-1} have been collected in hourly bins. The thick and thin vertical bars denote the interquartile range and 90th percentile of rain rate, respectively. The solid and dashed line indicate the median rain rate and mean rain occurrence frequency, respectively.

HESSD

7, 6351–6380, 2010

Title Page
Abstract | Introduction
Conclusions | References
Tables | Figures
◀| |▶
◀ ▶
Back | Close
Full Screen / Esc
Printer-friendly Version
Interactive Discussion

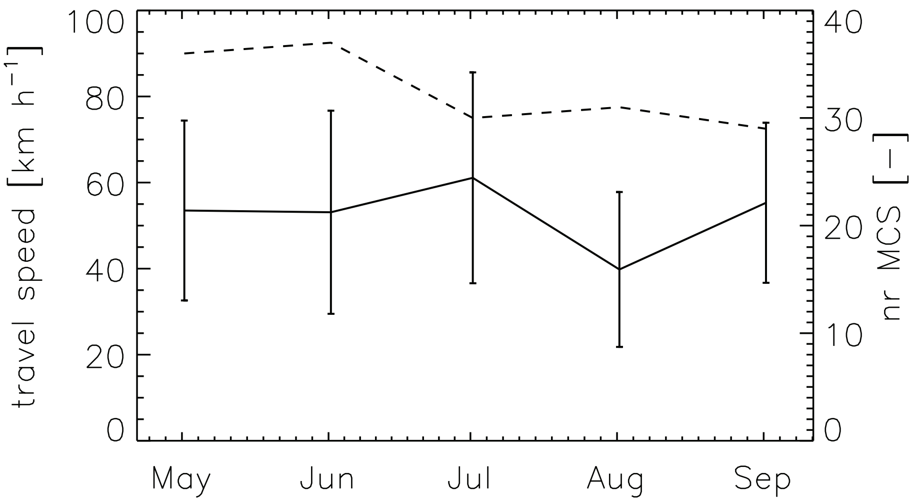

Fig. 6. Monthly mean daytime westward MCS travel speed (solid line), standard deviation (error bars), and the corresponding number of MCSs (dashed line) over the West African continental area (7°–20° N, 12° W–20° E) for May–September 2006. Note that in both August and September a data gap of 7 days occurred, which impacts the number of detected MCSs for these months.

HESSD
7, 6351–6380, 2010

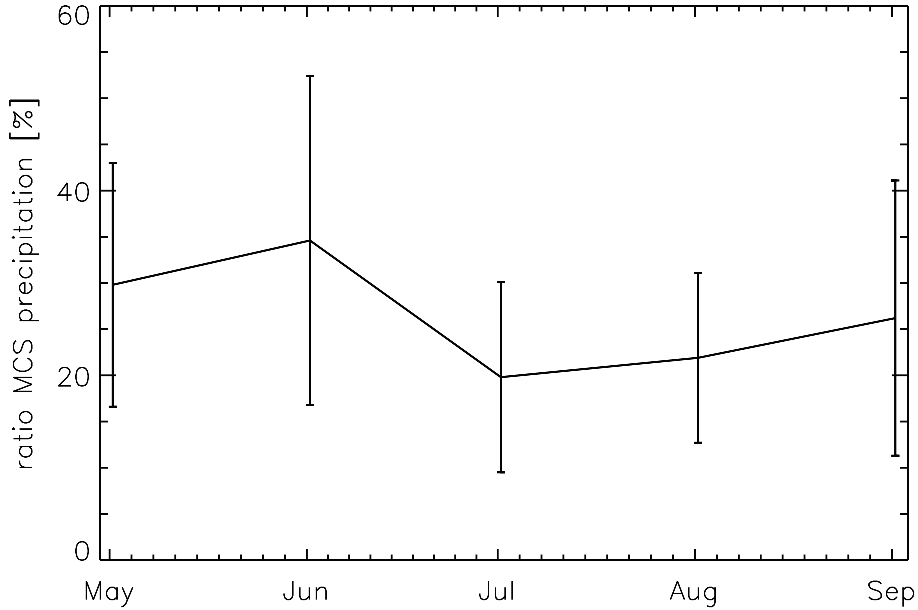

Fig. 7. Monthly mean daytime MCS precipitation ratio calculated from 163 MCSs, with error bars denoting the standard deviation.

HESSD

7, 6351–6380, 2010

Rainfall monitoring West-Africa with SEVIRI

E. L. A. Wolters et al.

Title Page
Abstract | Introduction
Conclusions | References
Tables | Figures
◀| |▶
◀ ▶
Back | Close
Full Screen / Esc
Printer-friendly Version
Interactive Discussion